Second Harmonic Generation from a Single Plasmonic Nanorod Strongly Coupled to a WSe_2 Monolayer

Chentao Li†, Xin Lu†, Ajit Srivastava†, S. David Storm§, Rachel Gelfand§, Matthew Pelton§, Maxim Sukharev‡, ‖, Hayk Harutyunyan*†

†Department of Physics, Emory University, 400 Dowman Dr., Atlanta, Georgia 30324, United States

§Department of Physics, UMBC (University of Maryland, Baltimore County), 1000 Hilltop Circle, Baltimore, Maryland 21250, United States

‡College of Integrative Sciences and Arts, Arizona State University, Mesa, Arizona 85212, United States

‖Department of Physics, Arizona State University, Tempe, Arizona 85287, United States

Supporting Information Placeholder

ABSTRACT: Monolayer transition metal dichalcogenides, coupled to metal plasmonic nanocavities, have recently emerged as new platforms for strong light-matter interactions. These systems are expected to have nonlinear-optical properties that will enable them to be used as entangled photon sources, compact wave-mixing devices, and other elements for classical and quantum photonic technologies. Here we report the first experimental investigation of the nonlinear properties of these strongly-coupled systems, by observing second harmonic generation from a WSe_2 monolayer strongly coupled to a single gold nanorod. The pump-frequency dependence of the second-harmonic signal displays a pronounced splitting that can be explained by a coupled-oscillator model with second-order nonlinearities. Rigorous numerical simulations utilizing a non-perturbative nonlinear hydrodynamic model of conduction electrons support this interpretation and reproduce experimental results. Our study thus lays the groundwork for understanding the nonlinear properties of strongly-coupled nanoscale systems. **KEYWORDS:** *plasmon-exciton polaritons, strong coupling, transition metal dichalcogenides, nonlinear optics, second harmonic generation, Rabi splitting*

The development of cavity quantum electrodynamics (QED) has provided new control over light-matter interaction.[1] The Purcell effect was the first demonstration of such control, showing that spontaneous emission can be modified by changing the photonic density of states of the environment. When the rate, Ω, at which energy is exchanged between cavity photons and emitters (known as the vacuum Rabi frequency) is faster than any decay process in the system, the emitter excitation and cavity photons form new, hybridized states known as polaritons.[2-4] These polaritons have enabled novel phenomena such as control of the optical Stark effect[5], polariton lasing[6], polariton condensation,[7] and control of chemical reactivity.[8, 9] Besides these fundamental phenomena, the strongly coupled systems also have the potential to enable applications in optoelectronic devices, optical sensors, and quantum computing.[10, 11 12-15]

To reach the strong coupling regime, early experiments typically used high-quality-factor dielectric cavities such as Fabry-Perot resonators[16, 17], photonic crystals[18], whispering-gallery-mode resonators[19], and distributed-Bragg-reflector cavities[20], with relatively large mode volumes restricted by the diffraction limit of light $\sim(\lambda/2n)^3$. By contrast, metal plasmonic nanocavities such as single nanospheres[21] and nanorods (NR)[22] are not subject to the diffraction limit and provide deeply subwavelength interaction volumes.

Several material platforms have been used for strong coupling to plasmonic nanocavities, including quantum dots and molecular excitons.[17, 23-28] Recent progress in the fabrication and characterization of transition metal dichalcogenides (TMDs) has enabled several demonstrations of strong coupling between plasmons and excitons in these TMDs.[21, 29-35] A particular advantage of these materials is their large exciton binding energy, which enables strong plasmon-exciton coupling at room temperature.[36] Furthermore, the two-dimensional geometry of these materials results in large in-plane dipole moments in the interaction area, significantly increasing coupling with the cavity mode.

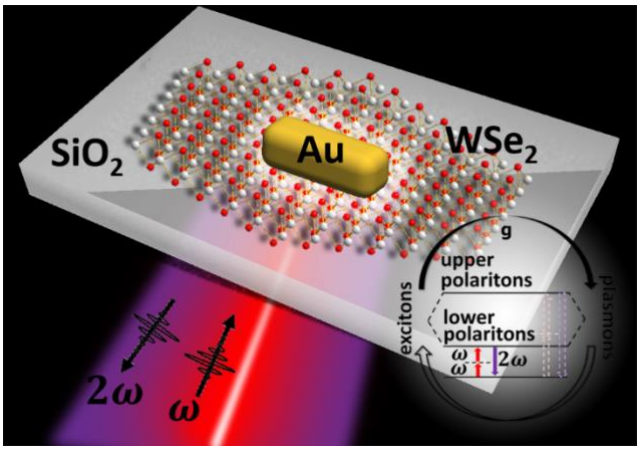

Figure 1. Schematic of the experimental setup. An isolated gold nanorod is strongly coupled to a monolayer of WSe_2 on a glass substrate. The second-harmonic signal at frequency 2ω, excited by a fundamental beam at frequency ω, is collected in the epi-illumination configuration.

So far, studies of these systems have been limited to their linear optical response. However, their nonlinear optical response has the potential to provide new routes for the development of nanoscale optoelectronic devices. For example, the nonlinearities may enable efficient entangled photon generation, compact wave mixing, and phenomena essential for optical quantum technologies and nanophotonic platforms. Additionally, the nonlinear signals can be potentially used to learn about the properties of underlying electronic states of the system, e.g. by probing the symmetries of polaritonic wavefunctions.

Nonlinear signal generation in the strongly-coupled regime has been studied using various platforms. For example, previous

studies have focused on second harmonic generation (SHG) from exci-

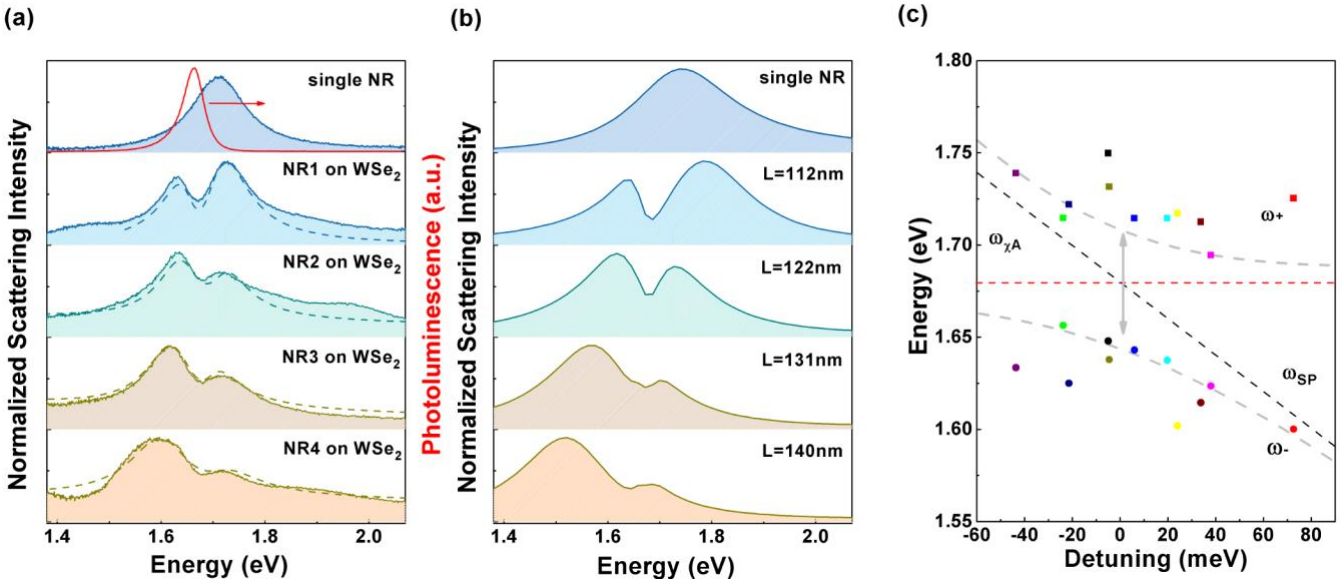

Figure 2. (a) Measured photoluminescence spectrum of a monolayer of WSe_2 (red, top panel), and measured dark-field-scattering spectra of an isolated gold nanorod (top panel) and of single nanorods coupled to the same WSe_2 monolayer (bottom panels). Dashed lines are fits using the linear coupled-oscillator model. (b) Calculated dark-field scattering spectra of an isolated gold nanorod (top panel, length is 112 nm and diameter is 40 nm) and of nanorods with different lengths coupled to a WSe_2 monolayer (bottom panels). (c) Frequencies of upper polaritons (solid squares) and lower polaritons (solid circles) extracted from fits to experimental data. Points with the same colors correspond to frequencies from the same scattering spectra. Grey lines are fitting results using the coupled-oscillator model, showing the anti-crossing behavior characteristic of strong coupling.

tons coupled to GaAs microcavities[37, 38] and third harmonic generation (THG) enhancement has been observed from polymethine dye-microcavity coupled systems.[39] Furthermore, SHG enhancement from WS_2-Ag nanocavity systems has been reported in the

weak-coupling regime.[40] Finally, in Ref. 17, a splitting of pump-dependent SHG spectral peaks due to the formation of polaritonic states was observed for J-aggregates embedded in Fabry-Perot (FP) cavities. However, to our knowledge, no work has previously studied nonlinear signal generation from plasmon-exciton polaritons in a single nanocavity.

Here, we experimentally demonstrate second-harmonic generation (SHG) from single gold NRs coupled to a monolayer of WSe_2. The pump-frequency-dependent nonlinear signal shows a distinct spectral splitting. Numerical simulations and a simple analytic model show that this splitting can be attributed to formation of hybridized polaritonic states between plasmons and excitons in the TMD monolayer.

A schematic of the coupled system, which consists of a monolayer of WSe_2 and a single gold NR on top, is depicted in Figure 1. The sample is fabricated on a glass coverslip. (See Methods for details on sample fabrication).

The TMD monolayers are identified by raster scanning the sample and detecting the photoluminescence (PL) signal in a confocal configuration at room temperature (see Supporting Information Figure S1). The PL intensity is highly sensitive to the number of TMD layers, and only monolayers feature a direct bandgap and strong emission;[41-43] an example of PL from a WSe_2 monolayer is shown in Figure 2 (a). A pronounced peak around 1.66eV is clearly observed, corresponding to emission from A excitons[41].

The gold NRs are designed to support longitudinal plasmonic resonances around 1.66eV, matching the A-exciton transition. Excitation of these plasmon modes give rise to confined in-plane electric fields at the surface of the WSe_2 flake, enabling coupling to excitons in the TMD. Figure 2 (a) shows examples of dark-field scattering spectra from an isolated gold NR and from individual NRs coupled to WSe_2 monolayers. The scattering spectra of the coupled systems show two peaks, as expected for the strong-coupling regime (See Methods for details on optical measurements).

To unambiguously attribute the scattering spectral peaks to exciton-plasmon polaritons, Au NRs of different lengths, and thus different longitudinal plasmon frequencies, are investigated numerically (see Figure 2 (a) and Supporting Information Figure S2). Finite difference time domain (FDTD) simulations of the coupled systems' scattering spectra give results very similar to the experimental data, as illustrated in Figure 2 (b). (Parameters of the numerical simulations are provided in Supplemental Information.)

The linear scattering spectra can also be fit to a simple classical model, where the dipole moments, μ_{pl} and μ_{ex}, of the plasmon and the exciton are represented as a pair of coupled harmonic oscillators:[44-46]

$$\ddot{\mu}_{pl} + \gamma_{pl}\dot{\mu}_{pl} + \omega_{pl}^2\mu_{pl} = F_o + g\left(\omega_{pl}d_{pl}/d_{ex}\right)\mu_{ex} \quad (1)$$

$$\ddot{\mu}_{ex} + \gamma_{ex}\dot{\mu}_{ex} + \omega_{ex}^2\mu_{ex} = g\left(\omega_{ex}d_{ex}/d_{pl}\right)\mu_{pl} \quad (2)$$

where γ_{pl} is the linewidth of the plasmon; ω_{pl} is the resonance frequency of the plasmon; d_{pl} is the polarizability of the plasmon; γ_{ex}, ω_{ex}, and d_{ex} are the corresponding terms for the exciton in WSe_2; and g is the effective coupling strength between the plasmon and exciton. The external field is assumed to produce a driving force, F_o, on only the plasmon, because its polarizability is much greater than that of the exciton. The larger polarizability of the plasmon also means that only its dipole contributes to the scattering cross-section σ_{scat}:

$$\sigma_{scat} \propto \left|\omega^2\mu_{pl}^{(1)}\right|^2 \quad (3)$$

with the steady-state solution for the dipole given by

$$\mu_{pl} = \frac{F_o(\omega_{ex}^2 - \omega^2 - i\omega\gamma_{ex})}{(\omega_{ex}^2 - \omega^2 - i\omega\gamma_{ex})(\omega_{pl}^2 - \omega^2 - i\omega\gamma_{pl}) - \omega_{ex}\omega_{pl}g^2} \quad (4)$$

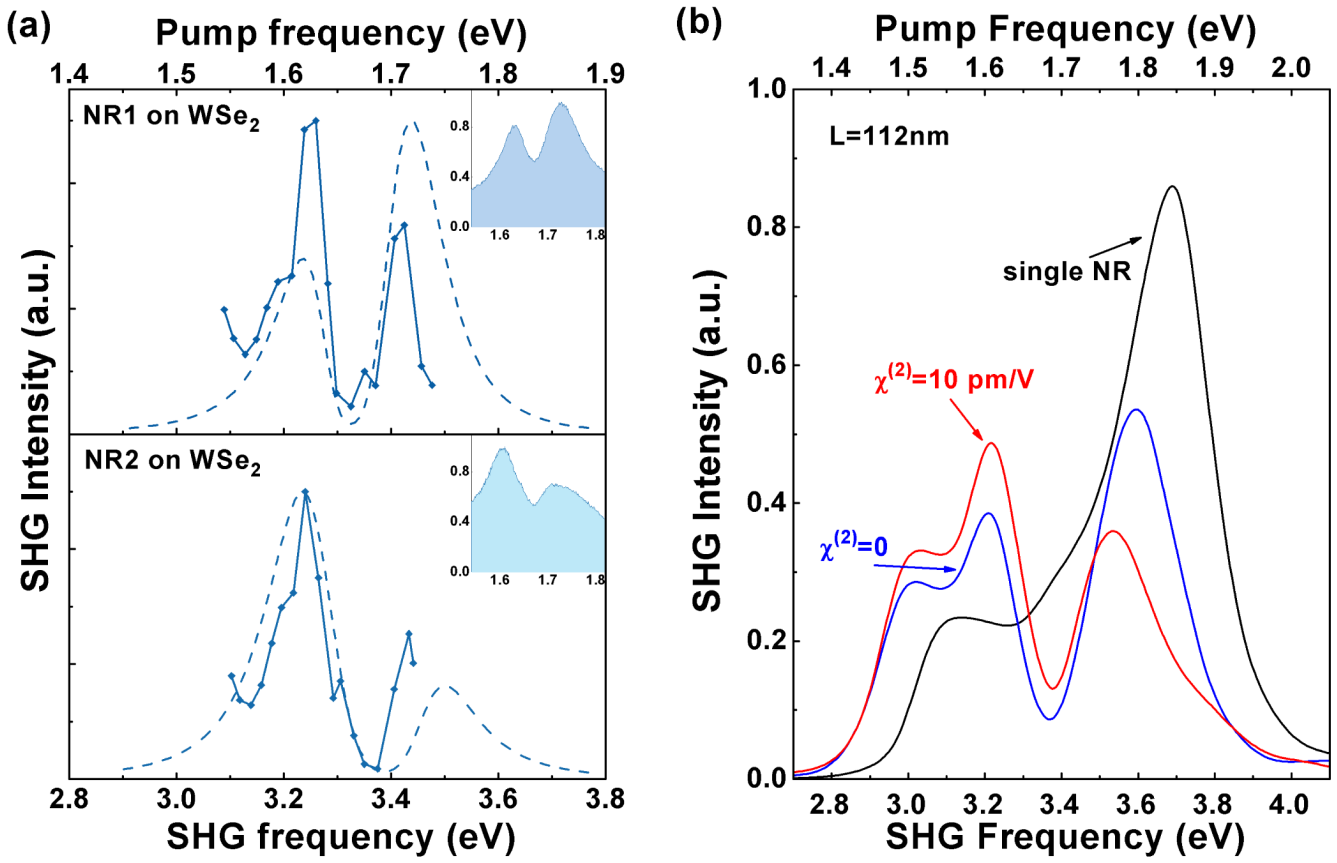

Figure 3. (a) Second-harmonic signals measured at different pump frequencies for single gold nanorods on a WSe_2 monolayer (solid lines). The corresponding linear scattering spectra are shown in the insets. Dashed lines show fitting results using the nonlinear coupled-oscillator model. (b) Calculated second-harmonic spectra for a single nanorod (length is 112nm, black) and the nanorod-WSe_2 coupled system using $\chi^{(2)} = 0$ (blue) and $\chi^{(2)} = 10$ pm/V (red) for WSe_2.

and γ_{ex} and ω_{ex} are constrained to be near the values obtained from the photoluminescence spectrum of the bare WSe_2 layer; the only free parameters in the fits are thus the coupling strength g and an arbitrary overall scaling factor.

From the fitted parameters, the real frequencies of the coupled plasmon-exciton modes can be calculated according to[46, 47]

$$\omega_{\pm} = \frac{1}{2}(\omega_{pl} + \omega_{ex}) \pm \sqrt{g^2 + \frac{1}{4}(\omega_{pl} - \omega_{ex})^2} \quad (5)$$

In Figure 2 (c), we plot $\omega_{\pm}$ as functions of the detuning $\delta \equiv \omega_{ex} - \omega_{pl}$, demonstrating the characteristic anti-crossing behavior. From this plot, we obtain an average coupling strength $g = 80 \pm 13$ meV. Comparing to the fitted ranges of plasmon linewidth, $\gamma_{pl} = 105 - 150$ meV and the exciton linewidth $\gamma_{ex} \approx 70$ meV, we can see that the coupled plasmon-WSe_2 system meets the strong-coupling criterion[4, 46]

$$g > \frac{1}{4}(\gamma_{pl} + \gamma_{ex}) \quad (6)$$

We now turn our attention to the nonlinear properties of the sample by performing SHG measurements in a confocal configuration. The spectral dependence of the integrated SHG signal as a function of excitation wavelength is shown for two representative systems in Figure 3 (a). These SHG spectra exhibit two distinct peaks, which match well with the positions of the peaks in the linear scattering spectra (Figure 3 (a), shaded areas). This indicates that the emitted second harmonic has its origins in the coupled system, rather than in either the gold NR or the WSe_2 separately.

Figure 2 (a) shows sample fits of the experimental data to Eqs. (3) and (4). In these fits, γ_{pl} and ω_{pl} are contstrained to be within the range measured for scattering from gold NRs uncoupled to WSe_2,

The measured SHG spectra can be understood intuitively by extending the coupled-harmonic-oscillator model of Eqs. (1) and (2) to include second-order nonlinear terms:[48]

$$\ddot{\mu}_{pl} + \gamma_{pl}\dot{\mu}_{pl} + \omega_{pl}^2\mu_{pl} + a\mu_{pl}^2 = F_o + g(\omega_{pl}d_{pl}/d_{ex})\mu_{ex} \quad (7)$$

$$\ddot{\mu}_{ex} + \gamma_{ex}\dot{\mu}_{ex} + \omega_{ex}^2\mu_{ex} + b\mu_{ex}^2 = g(\omega_{ex}d_{ex}/d_{pl})\mu_{pl} \quad (8)$$

where a and b are proportional to the second-order nonlinear susceptibility of Au and WSe_2, respectively. These coupled nonlinear equations can be solved in the perturbation limit[49]

$$\mu_{pl} = \mu_{pl}^{(1)}e^{i\omega t} + \mu_{pl}^{(2)}e^{2i\omega t} + \cdots \quad (9)$$

$$\mu_{ex} = \mu_{ex}^{(1)}e^{i\omega t} + \mu_{ex}^{(2)}e^{2i\omega t} + \cdots \quad (10)$$

The linear terms $\mu_{pl}^{(1)}$ and $\mu_{ex}^{(1)}$ are the same as the solutions to the linear equations, Eqs. (1) and (2), whereas the second-order terms are given by

$$\mu_{pl}^{(2)} = \frac{aF_o^2(\omega_{ex}^2 - \omega^2 - i\omega\gamma_{ex})^2}{(\omega_{pl}^2 - (2\omega)^2 - i\omega\gamma_{pl})\left[(\omega_{ex}^2 - \omega^2 - i\omega\gamma_{ex})(\omega_{pl}^2 - \omega^2 - i\omega\gamma_{pl}) - \omega_{ex}\omega_{pl}g^2\right]^2} \quad (11)$$

and

$$\mu_{em}^{(2)} = \frac{bF_o^2\left(g\omega_{ex}d_{ex}/d_{pl}\right)^2}{(\omega_{ex}^2-(2\omega)^2-i\omega\gamma_{ex})\left[(\omega_{ex}^2-\omega^2-i\omega\gamma_{ex})\left(\omega_{pl}^2-\omega^2-i\omega\gamma_{pl}\right)-\omega_{ex}\omega_{pl}g^2\right]^2} \quad (12)$$

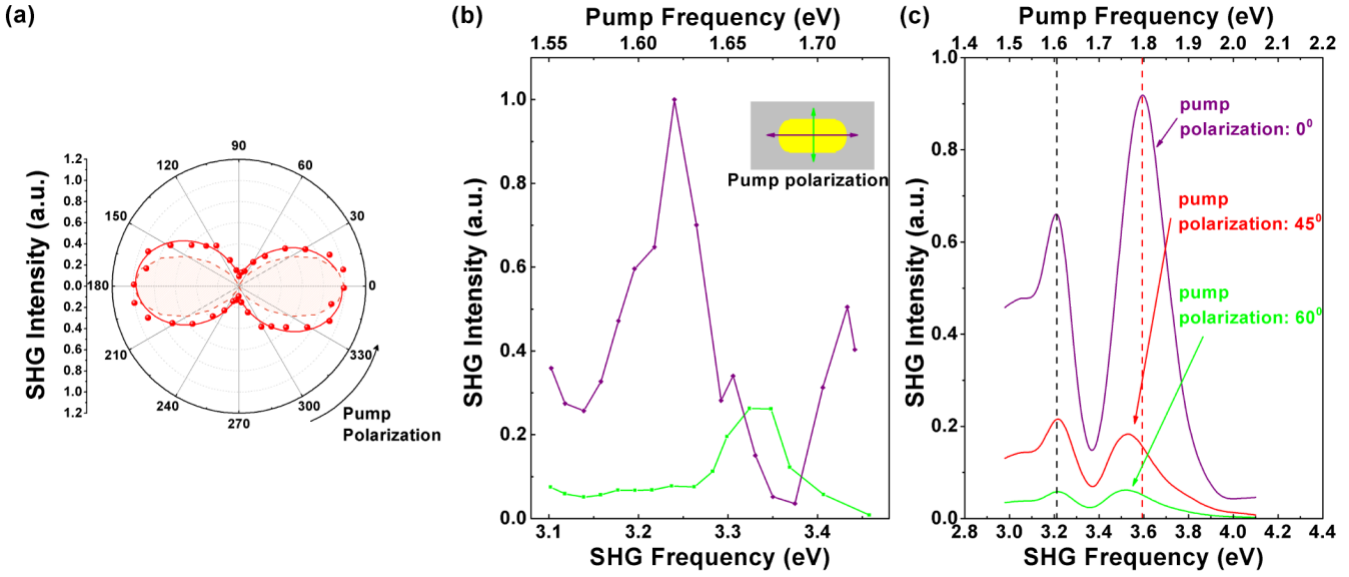

Figure 4. (a) Measured pump-polarization-dependent second-harmonic radiation pattern from the nanorod-WSe_2 coupled system (red dots) and a dipolar emission fit (solid red line). The numerical calculation results under the same condition are also shown (orange dashed line and filled area). (b) Measured second-harmonic spectra for the nanorod-WSe_2 system when pumping longitudinally (violet) and transversely (green) relative to the long axis of the nanorod. (c) Calculated second-harmonic spectra of a nanorod (length is 112nm) strongly coupled to WSe_2 when pumping with different polarization angles relative to the long axis of the nanorod.

The second-order (hyper-Rayleigh) scattering cross-section is given by

$$\sigma_{SHG} \propto \left|\omega^2\mu_{pl}^{(2)}\right|^2 + \left|\omega^2\mu_{ex}^{(2)}\right|^2 \quad (13)$$

For the same reason that we neglect linear scattering from WSe_2, we neglect the second term in Eq. (13) when comparing to experimental SHG spectra. This means that all the parameters in the fit to a given SHG spectrum are constrained by the fit to the corresponding linear spectrum, and the only free parameter is an arbitrary overall scaling factor. In practice, we account for possible calibration errors in the measurement of the SHG spectrum by including an offset and scaling factor for the frequency axis in the fit.

Fit results are shown in Figure 3 (a). The coupled-nonlinear-oscillator model shows good qualitative agreement with the measured SHG spectra. Quantitative differences are most likely due to errors in measuring SHG intensity at the edge of the spectral range of the detector used experimentally.

To confirm the validity of this simple physical picture, we also compare experimental SHG spectra to those obtained by numerically solving a non-perturbative fully vectoral hydrodynamic model coupled to Maxwell's equations[48]. Calculation results are shown in Figure 3 (b), and clearly reproduce the observed spectral splitting. We also use these simulations to compare SHG from the coupled system when we include a realistic nonlinear coefficient for the WSe_2 monolayer, and when we neglect the nonlinearity of this material. The differences in the SHG excitation spectra are small, demonstrating that the SHG arises primarily from the surface nonlinearity of the gold nanoparticle, and justifying our neglect of the second term in Eq. (13). Moreover, the splitting in the SHG spectrum is unaffected by the source of the nonlinearity, showing that the emitted second harmonic arises from the polaritons, and not from the plasmons or excitons separately.

Including the second-order nonlinearity of WSe_2 in the simulations noticeably reduces the separation between the peaks in the SHG spectrum. This is in agreement with the coupled-nonlinear-oscillator model, which predicts a smaller splitting in the SHG spectrum due to the exciton dipole (Eq. (12)) than in the SHG spectrum due to the plasmon dipole (Eq. (11)). Since the total spectrum is a weighted sum of the exciton and plasmon spectra, increasing the fraction of SHG emitted by the exciton will reduce the overall peak separation.

All the calculated SHG spectra show an additional broad peak near 1.6 eV. Part of this peak can also be seen in the experimental spectra, near the edge of the experimentally accessible frequency range. This peak is attributed to local field enhancement at the tips of the rod. Further numerical details of the model, near-field distributions at the fundamental and harmonic frequencies, and additional simulations including third harmonic response are provided in the Supporting Information (Figures S5-S9).

Finally, we discuss the polarization dependence of the SHG spectra. The experimentally measured radiation pattern for a representative strongly-coupled system is shown in Figure 4 (a) along with results of the corresponding numerical calculation. A dipolar SHG emission pattern is observed, corresponding to the longitudinal plasmonic mode radiation.[50]

The fact that the dipolar emission pattern arises from the longitudinal plasmon can be seen from the following argument. The horizontal component of the second order macroscopic polarization can be written as:

$$P_x^{(2)}(2\omega) \sim \chi_{xxx}^{(2)} cos^2(\theta) + \chi_{xyy}^{(2)} sin^2(\theta) \quad (14)$$

where $\chi_{ijk}^{(2)}$ is the second order susceptibility tensor and θ is the in-plane polarization of the pump. It is clear from Fig. 4 (a) that the SHG signal has a dominant horizontal component, indicating that $\chi_{xxx}^{(2)} \gg \chi_{xyy}^{(2)}$.

In Figure 4 (b) we show SHG spectra recorded for longitudinal and transverse polarization of the pump beam. It can be clearly seen that a longitudinally-polarized pump excites the polaritonic states due to coupling between the longitudinal plasmon and the WSe_2 excitons. Meanwhile, the transverse pump produces signal only at the exciton peak, the intensity of which is 4 times smaller than that of the polariton peaks. Similar trends are seen for the numerical simulations, as shown in Figure 4 (c). Specifically, maximum splitting in the SHG excitation spectrum is seen when the pump polarization is aligned along the long axis of the nanorod. Rotating away from this orientation decreases the splitting in the SHG spectrum; the upper-polariton peak is more affected than the lower-polariton peak, because the non-zero detuning between the plasmon and exciton means that the two polariton branches have unequal plasmonic character.

In conclusion, we report the experimental observation of Rabi splitting in the pump-frequency-dependent SHG signals from a strongly coupled system consisting of a gold nanorod and a monolayer of WSe_2. As described by FDTD simulations based on the non-perturbative hydrodynamic-Maxwell model, these polaritons reshape the SHG response of the system by creating local field enhancement at the polariton frequencies. The theory and simulations can be described using a simple, analytical model of two coupled nonlinear classical oscillators. Future work will be dedicated to extending the studies to nonlinear-optical effects beyond SHG, such as wave mixing and nonlinear extinction, and to plasmonic and excitonic systems with more complex symmetry properties. This, in turn, will pave the way for devices such as integrated entangled photon sources, room temperature quantum repeaters, and wave mixing elements.

Methods

Atomically thin layers of WSe_2 are mechanically exfoliated to a PDMS tape and then transferred to glass coverslips. Before transfer, the coverslips are ultrasonically cleaned in soap, de-ionized water, acetone, and IPA for 20 minutes in each solvent and are then dried using nitrogen. This method ensures the single crystalline structure of each WSe_2 flake.

To add gold NRs on top of the flake, we adopt the drop casting method described in Ref. 21. An aqueous solution of colloidal gold NRs with a diameter of 40 nm and an average length of 112 nm (Nanopartz Inc.) is 20-fold diluted with deionized water and sonicated to reduce aggregation. It should be noted that the lengths of nanorods in the solution are distributed around the average length, so that the plasmon resonances of different individual rods will have different detunings relative to the exciton transition frequency in WSe_2. 1 μL of the diluted NR solution is then drop-cast onto the substrate with the WSe_2 flake and is washed off with deionized water after 1 min. These casting parameters result in around 30 NRs on each several-micron-sized WSe_2 flake. The NRs are functionalized as synthesized with a CTAB layer, which acts as a spacer between gold NRs and the WSe_2 flake to avoid charge transfer.

For PL measurements, a 50x objective (NA=0.5) is used to focus a 633-nm HeNe excitation laser beam on the sample and to collect PL signal in the epi-illumination configuration. PL maps are obtained by raster scan of the sample using an XY piezo stage and collecting the PL signal with an avalanche photodiode (APD). The scanning maps of several monolayer flakes are shown in the Supporting Information (Figure S1).

Scattering spectra are measured by focusing broadband light from a halogen lamp on the sample using a dark-field condenser lens. A 50x objective (NA=0.5) is used to collect the scattered light while omitting the transmitted light.

For SHG measurements, a Chameleon Ultra II Ti:sapphire femtosecond laser with a repetition rate of 80 MHz is used as the excitation source. A 60x oil immersion objective (NA= 1.4) is used to confocally focus the excitation beam and collect the SHG signals. To avoid the influence of higher-order plasmonic modes, a paraxial beam with a diameter of 2 mm at the objective-lens back focal plane is used, ensuring near-normal incidence of the excitation laser beam. On each NR candidate that shows a Rabi splitting in the dark field scattering spectra, nonlinear spectroscopy is performed by continuously tuning the pump from 700 nm to 800nm (3.1 eV – 3.6 eV) and recording the SHG spectrum for every excitation wavelength. To remove the broadband emission due to two-photon photoluminescence[51, 52], the raw SHG spectrum at each pump wavelength is fitted with a second order polynomial background and a sharp Gaussian peak (Supporting Information Figure S3). The area under the Gaussian peak is taken to be the intensity of the SHG signal. The quadratic dependence of the SHG signal on the excitation power is verified experimentally (Supporting Information Figure S4). To measure polarization-dependent SHG signals, we use a Berek compensator to rotate the linear polarization of the excitation beam while integrating the polarization of the emitted signal.

ASSOCIATED CONTENT

Supporting Information

Photoluminescence maps and spectra, dark-field scattering spectra, procedure for integrating experimental second-harmonic spectra, SHG power-dependence data, nonlinear hydrodynamic model details, discussion of calculated SHG spectra, third-harmonic generation calculations, spatial distribution of near fields at fundamental and SHG frequencies, discussion of the effect of detuning on second-harmonic signals.

AUTHOR INFORMATION

Corresponding Author

hayk.harutyunyan@emory.edu

Author Contributions

H.H. conceived the project. C.L. performed the experiments. C.L., X.L. and A.S. fabricated the samples. D.S., R.G. and M.P. developed the analytical model. M.S. performed the numerical analysis. All authors contributed to the discussion of the results and the writing of the manuscript.

Notes

The authors declare no competing financial interests.

ACKNOWLEDGMENT

H.H. acknowledges support from the Department of Energy (DESC0020101). A.S. acknowledges support from NSF through the EFRI program-grant # EFMA-1741691 and NSF DMR award # 1905809. M.P. acknowledges support from the U.S. National Science Foundation (DMR-1905135). The computational part of this work is sponsored by the Air Force Office of Scientific Research under Grant No. FA9550-19-1-0009. The authors are grateful to Dr. Ruth Pachter and Prof. Stephan W. Koch for fruitful discussions pertaining to the optical response of WSe_2.

REFERENCES

(1) Merzbacher, E. *Quantum mechanics*; Wiley: New York, 1998.

(2) Sukharev, M.; Nitzan, A. Optics of exciton-plasmon nanomaterials. *J Phys Condens Matter* **2017,** 29, (44), 443003.

(3) Sanchez-Mondragon, J.; Narozhny, N.; Eberly, J. Theory of spontaneous-emission line shape in an ideal cavity. *Phys Rev Lett* **1983,** 51, (7), 550.
(4) Khitrova, G.; Gibbs, H.; Kira, M.; Koch, S. W.; Scherer, A. Vacuum Rabi splitting in semiconductors. *Nature Physics* **2006,** 2, (2), 81-90.
(5) Vasa, P.; Wang, W.; Pomraenke, R.; Maiuri, M.; Manzoni, C.; Cerullo, G.; Lienau, C. Optical Stark effects in J-aggregate–metal hybrid nanostructures exhibiting a strong exciton–surface-plasmon-polariton interaction. *Phys Rev Lett* **2015,** 114, (3), 036802.
(6) Christopoulos, S.; Von Högersthal, G. B. H.; Grundy, A.; Lagoudakis, P.; Kavokin, A.; Baumberg, J.; Christmann, G.; Butté, R.; Feltin, E.; Carlin, J.-F. Room-temperature polariton lasing in semiconductor microcavities. *Phys Rev Lett* **2007,** 98, (12), 126405.
(7) Deng, H.; Weihs, G.; Santori, C.; Bloch, J.; Yamamoto, Y. Condensation of semiconductor microcavity exciton polaritons. *Science* **2002,** 298, (5591), 199-202.
(8) Herrera, F.; Spano, F. C. Cavity-controlled chemistry in molecular ensembles. *Phys Rev Lett* **2016,** 116, (23), 238301.
(9) Thomas, A.; Lethuillier-Karl, L.; Nagarajan, K.; Vergauwe, R. M.; George, J.; Chervy, T.; Shalabney, A.; Devaux, E.; Genet, C.; Moran, J. Tilting a ground-state reactivity landscape by vibrational strong coupling. *Science* **2019,** 363, (6427), 615-619.
(10) Lodahl, P.; Mahmoodian, S.; Stobbe, S. Interfacing single photons and single quantum dots with photonic nanostructures. *Reviews of Modern Physics* **2015,** 87, (2), 347.
(11) Englund, D.; Majumdar, A.; Bajcsy, M.; Faraon, A.; Petroff, P.; Vučković, J. Ultrafast photon-photon interaction in a strongly coupled quantum dot-cavity system. *Phys Rev Lett* **2012,** 108, (9), 093604.
(12) Volz, T.; Reinhard, A.; Winger, M.; Badolato, A.; Hennessy, K. J.; Hu, E. L.; Imamoğlu, A. Ultrafast all-optical switching by single photons. *Nature Photonics* **2012,** 6, (9), 605-609.
(13) Sun, S.; Kim, H.; Solomon, G. S.; Waks, E. A quantum phase switch between a single solid-state spin and a photon. *Nat Nanotechnol* **2016,** 11, (6), 539-544.
(14) Sun, S.; Kim, H.; Luo, Z.; Solomon, G. S.; Waks, E. A single-photon switch and transistor enabled by a solid-state quantum memory. *Science* **2018,** 361, (6397), 57-60.
(15) Miscuglio, M.; Mehrabian, A.; Hu, Z.; Azzam, S. I.; George, J.; Kildishev, A. V.; Pelton, M.; Sorger, V. J. All-optical nonlinear activation function for photonic neural networks. *Optical Materials Express* **2018,** 8, (12), 3851-3863.
(16) Thompson, R.; Rempe, G.; Kimble, H. Observation of normal-mode splitting for an atom in an optical cavity. *Phys Rev Lett* **1992,** 68, (8), 1132.
(17) Chervy, T.; Xu, J.; Duan, Y.; Wang, C.; Mager, L.; Frerejean, M.; Munninghoff, J. A.; Tinnemans, P.; Hutchison, J. A.; Genet, C.; Rowan, A. E.; Rasing, T.; Ebbesen, T. W. High-Efficiency Second-Harmonic Generation from Hybrid Light-Matter States. *Nano Lett* **2016,** 16, (12), 7352-7356.
(18) Yoshie, T.; Scherer, A.; Hendrickson, J.; Khitrova, G.; Gibbs, H.; Rupper, G.; Ell, C.; Shchekin, O.; Deppe, D. Vacuum Rabi splitting with a single quantum dot in a photonic crystal nanocavity. *Nature* **2004,** 432, (7014), 200-203.
(19) Peter, E.; Senellart, P.; Martrou, D.; Lemaître, A.; Hours, J.; Gérard, J.; Bloch, J. Exciton-photon strong-coupling regime for a single quantum dot embedded in a microcavity. *Phys Rev Lett* **2005,** 95, (6), 067401.
(20) Reithmaier, J. P.; Sęk, G.; Löffler, A.; Hofmann, C.; Kuhn, S.; Reitzenstein, S.; Keldysh, L.; Kulakovskii, V.; Reinecke, T.; Forchel, A. Strong coupling in a single quantum dot–semiconductor microcavity system. *Nature* **2004,** 432, (7014), 197-200.
(21) Kleemann, M.-E.; Chikkaraddy, R.; Alexeev, E. M.; Kos, D.; Carnegie, C.; Deacon, W.; De Pury, A. C.; Große, C.; De Nijs, B.; Mertens, J. Strong-coupling of WSe 2 in ultra-compact plasmonic nanocavities at room temperature. *Nat Commun* **2017,** 8, (1), 1-7.
(22) Kern, J.; Trügler, A.; Niehues, I.; Ewering, J.; Schmidt, R.; Schneider, R.; Najmaei, S.; George, A.; Zhang, J.; Lou, J.; Hohenester, U.; Michaelis de Vasconcellos, S.; Bratschitsch, R. Nanoantenna-Enhanced Light–Matter Interaction in Atomically Thin WS2. *ACS Photonics* **2015,** 2, (9), 1260-1265.
(23) Zengin, G.; Wersäll, M.; Nilsson, S.; Antosiewicz, T. J.; Käll, M.; Shegai, T. Realizing strong light-matter interactions between single-nanoparticle plasmons and molecular excitons at ambient conditions. *Phys Rev Lett* **2015,** 114, (15), 157401.
(24) Wersäll, M.; Cuadra, J.; Antosiewicz, T. J.; Balci, S.; Shegai, T. Observation of mode splitting in photoluminescence of individual plasmonic nanoparticles strongly coupled to molecular excitons. *Nano Lett* **2017,** 17, (1), 551-558.
(25) Wiederrecht, G. P.; Wurtz, G. A.; Hranisavljevic, J. Coherent coupling of molecular excitons to electronic polarizations of noble metal nanoparticles. *Nano Lett* **2004,** 4, (11), 2121-2125.
(26) Schlather, A. E.; Large, N.; Urban, A. S.; Nordlander, P.; Halas, N. J. Near-field mediated plexcitonic coupling and giant Rabi splitting in individual metallic dimers. *Nano Lett* **2013,** 13, (7), 3281-3286.
(27) Roller, E.-M.; Argyropoulos, C.; Högele, A.; Liedl, T.; Pilo-Pais, M. Plasmon–exciton coupling using DNA templates. *Nano Lett* **2016,** 16, (9), 5962-5966.
(28) Liu, R.; Zhou, Z.-K.; Yu, Y.-C.; Zhang, T.; Wang, H.; Liu, G.; Wei, Y.; Chen, H.; Wang, X.-H. Strong light-matter interactions in single open plasmonic nanocavities at the quantum optics limit. *Phys Rev Lett* **2017,** 118, (23), 237401.
(29) Wen, J.; Wang, H.; Wang, W.; Deng, Z.; Zhuang, C.; Zhang, Y.; Liu, F.; She, J.; Chen, J.; Chen, H.; Deng, S.; Xu, N. Room-Temperature Strong Light-Matter Interaction with Active Control in Single Plasmonic Nanorod Coupled with Two-Dimensional Atomic Crystals. *Nano Lett* **2017,** 17, (8), 4689-4697.
(30) Li, B.; Zu, S.; Zhou, J.; Jiang, Q.; Du, B.; Shan, H.; Luo, Y.; Liu, Z.; Zhu, X.; Fang, Z. Single-nanoparticle plasmonic electro-optic modulator based on MoS2 monolayers. *ACS Nano* **2017,** 11, (10), 9720-9727.
(31) Stührenberg, M.; Munkhbat, B.; Baranov, D. G.; Cuadra, J.; Yankovich, A. B.; Antosiewicz, T. J.; Olsson, E.; Shegai, T. Strong light–matter coupling between plasmons in individual gold bi-pyramids and excitons in mono-and multilayer WSe2. *Nano Lett* **2018,** 18, (9), 5938-5945.
(32) Sun, J.; Hu, H.; Zheng, D.; Zhang, D.; Deng, Q.; Zhang, S.; Xu, H. Light-emitting plexciton: exploiting Plasmon–exciton interaction in the intermediate coupling regime. *ACS Nano* **2018,** 12, (10), 10393-10402.
(33) Wang, M.; Krasnok, A.; Zhang, T.; Scarabelli, L.; Liu, H.; Wu, Z.; Liz‐Marzán, L. M.; Terrones, M.; Alù, A.; Zheng, Y. Tunable fano resonance and plasmon‐exciton coupling in single au nanotriangles on monolayer WS2 at room temperature. *Adv Mater* **2018,** 30, (22), 1705779.
(34) Zheng, D.; Zhang, S.; Deng, Q.; Kang, M.; Nordlander, P.; Xu, H. Manipulating Coherent Plasmon-Exciton Interaction in a Single Silver Nanorod on Monolayer WSe2. *Nano Lett* **2017,** 17, (6), 3809-3814.
(35) Liu, X.; Galfsky, T.; Sun, Z.; Xia, F.; Lin, E.-c.; Lee, Y.-H.; Kéna-Cohen, S.; Menon, V. M. Strong light–matter coupling in two-dimensional atomic crystals. *Nature Photonics* **2014,** 9, (1), 30-34.
(36) Khurgin, J. B. Two-dimensional exciton–polariton—light guiding by transition metal dichalcogenide monolayers. *Optica* **2015,** 2, (8), 740-742.
(37) Schmutzler, J.; Aßmann, M.; Czerniuk, T.; Kamp, M.; Schneider, C.; Höfling, S.; Bayer, M. Nonlinear spectroscopy of exciton-polaritons in a GaAs-based microcavity. *Physical Review B* **2014,** 90, (7), 075103.
(38) Pimenta, A. C. S.; Faria, L. C.; González, J. C.; de Giorgi, M.; Sanvitto, D.; Matinaga, F. M. Nonlinear Optical Effects with Polariton Lasers in a GaAs Microcavity. *The Journal of Physical Chemistry C* **2018,** 122, (30), 17501-17506.
(39) Barachati, F.; Simon, J.; Getmanenko, Y. A.; Barlow, S.; Marder, S. R.; Kéna-Cohen, S. Tunable Third-Harmonic Generation from Polaritons in the Ultrastrong Coupling Regime. *ACS Photonics* **2018,** 5, (1), 119-125.
(40) Han, X.; Wang, K.; Persaud, P. D.; Xing, X.; Liu, W.; Long, H.; Li, F.; Wang, B.; Singh, M. R.; Lu, P. Harmonic Resonance Enhanced Second-Harmonic Generation in the Monolayer WS2–Ag Nanocavity. *ACS Photonics* **2020,** 7, (3), 562-568.
(41) Wang, Z.; Dong, Z.; Zhu, H.; Jin, L.; Chiu, M. H.; Li, L. J.; Xu, Q. H.; Eda, G.; Maier, S. A.; Wee, A. T. S.; Qiu, C. W.; Yang, J. K. W. Selectively Plasmon-Enhanced Second-Harmonic Generation from Monolayer Tungsten Diselenide on Flexible Substrates. *ACS Nano* **2018,** 12, (2), 1859-1867.
(42) Splendiani, A.; Sun, L.; Zhang, Y.; Li, T.; Kim, J.; Chim, C.-Y.; Galli, G.; Wang, F. Emerging photoluminescence in monolayer MoS2. *Nano Lett* **2010,** 10, (4), 1271-1275.
(43) Mak, K. F.; Lee, C.; Hone, J.; Shan, J.; Heinz, T. F. Atomically thin MoS 2: a new direct-gap semiconductor. *Phys Rev Lett* **2010,** 105, (13), 136805.
(44) Rudin, S.; Reinecke, T. Oscillator model for vacuum Rabi splitting in microcavities. *Physical Review B* **1999,** 59, (15), 10227.
(45) Wu, X.; Gray, S. K.; Pelton, M. Quantum-dot-induced transparency in a nanoscale plasmonic resonator. *Opt Express* **2010,** 18, (23), 23633-23645.

(46) Pelton, M.; Storm, S. D.; Leng, H. Strong coupling of emitters to single plasmonic nanoparticles: exciton-induced transparency and Rabi splitting. *Nanoscale* **2019,** 11, (31), 14540-14552.

(47) Jaynes, E. T.; Cummings, F. W. Comparison of quantum and semiclassical radiation theories with application to the beam maser. *Proceedings of the IEEE* **1963,** 51, (1), 89-109.

(48) Drobnyh, E.; Pachter, R.; Sukharev, M. Harmonic generation by metal nanostructures optically coupled to two-dimensional transition-metal dichalcogenide. *The Journal of Physical Chemistry C* **2019,** 123, (11), 6898-6904.

(49) Boyd, R. W. *Nonlinear optics*; Elsevier, AP Academic Press: London, 2020.

(50) Butet, J.; Bernasconi, G. D.; Petit, M.; Bouhelier, A.; Yan, C.; Martin, O. J. F.; Cluzel, B.; Demichel, O. Revealing a Mode Interplay That Controls Second-Harmonic Radiation in Gold Nanoantennas. *ACS Photonics* **2017,** 4, (11), 2923-2929.

(51) Butet, J.; Duboisset, J.; Bachelier, G.; Russier-Antoine, I.; Benichou, E.; Jonin, C.; Brevet, P. F. Optical second harmonic generation of single metallic nanoparticles embedded in a homogeneous medium. *Nano Lett* **2010,** 10, (5), 1717-21.

(52) Slablab, A.; Le Xuan, L.; Zielinski, M.; de Wilde, Y.; Jacques, V.; Chauvat, D.; Roch, J.-F. Second-harmonic generation from coupled plasmon modes in a single dimer of gold nanospheres. *Opt Express* **2012,** 20, (1), 220-227.

Table of Contents Graphic